



Sulfur vacancy engineering of MoS₂ via phosphorus incorporation for improved electrocatalytic N₂ reduction to NH₃

Hao Fei^a, Ting Guo^a, Yue Xin^a, Liangbing Wang^{a,b,*}, Ruoqi Liu^a, Dezhi Wang^{a,b}, Fangyang Liu^c, Zhuangzhi Wu^{a,b,*}

^a School of Materials Science and Engineering, Central South University, Changsha 410083, China

^b Key Laboratory of Ministry of Education for Non-ferrous Materials Science and Engineering, Changsha 410083, China

^c School of Metallurgy and Environment, Central South University, Changsha 410083, China



ARTICLE INFO

Keywords:

Molybdenum disulfide
Sulfur vacancy
Electrocatalysis
Nitrogen reduction reaction
Hydrogen evolution reaction

ABSTRACT

Electrocatalytic N₂ reduction reaction (NRR) serves as a promising approach for converting N₂ to NH₃ in a sustainable way to replace the energy-intensive Haber-Bosch process. MoS₂-based electrocatalysts hold great potentials in catalyzing N₂ reduction due to their similarity with active MoFe-co in biological nitrogenase. In this work, we reported a sulfur vacancy-rich MoS₂ as an excellent electrocatalyst for NRR, where the sulfur vacancies (SVs) were easily controlled by regulating the amount of P dopants. MoS₂ with abundant SVs (P-M-1) achieved a large NH₃ yield rate of 60.27 $\mu\text{g h}^{-1} \text{mg}^{-1}_{\text{cat.}}$ and high Faradaic efficiency of 12.22% towards NRR. Further mechanistic study revealed that P dopants not only created SVs as the active centers but also modulated the electronic structure for the enhanced adsorption and activation of N₂ molecules, thus immensely promoting the catalytic performance of NRR.

1. Introduction

As a green fuel and an attractive carbon-neutral hydrogen energy carrier with a high-energy density, ammonia (NH₃) plays an essential role in the development of modern industry and agriculture [1–4]. Owing to the intrinsic inertness of N₂ molecules, industrial-scale synthesis of NH₃ still depends on traditional Haber-Bosch process under high temperature and pressure, which induces large energy consumption and severe release of CO₂ [5–7]. As an alternative, emerging electrocatalytic N₂ reduction reaction (NRR) offers a promising opportunity to convert N₂ to NH₃ under mild conditions, but relies on high-performance catalysts [8,9].

Mimicking the MoFe-co in natural nitrogenase, molybdenum disulfide (MoS₂) has attracted particular attention in catalyzing the reduction of N₂ [10–18]. Thanks to the efforts of numerous research groups, a series of MoS₂-based modified electrodes have been designed and applied to the electrochemical fixation of N₂. Sun et al. initially reported that MoS₂ nanosheets exhibited a good activity for the NRR under neutral conditions with a high NH₃ yield rate of 13.09 $\mu\text{g h}^{-1} \text{mg}^{-1}_{\text{cat.}}$ and a FE of 1.17% at – 0.5 V vs. reversible hydrogen electrode (RHE) in 0.1 M Na₂SO₄ [19]. Afterword, defects were also constructed in MoS₂

via regulating the contents of sulfur (S) by them, which boosted the catalytic activity and selectivity of electrocatalytic N₂ reduction to NH₃ (NH₃ yield rate: 29.28 $\mu\text{g h}^{-1} \text{mg}^{-1}_{\text{cat.}}$, FE: 8.34%) [20]. Li et al. loaded MoS₂ nanosheet on reduced graphene oxide (MoS₂-rGO) for electrocatalytic NRR, which achieved a high NH₃ yield rate of 24.82 $\mu\text{g h}^{-1} \text{mg}^{-1}_{\text{cat.}}$ and a Faraday efficiency (FE) of 4.58% at – 0.40 V vs. (RHE) in 0.1 M LiClO₄ [21]. Although some exploratory works have been done, MoS₂-based electrocatalysts with superior catalytic performance are still urgently needed.

Herein, we successfully constructed and regulated SVs in MoS₂ by introducing P dopants for electrocatalytic NRR. The obtained P-doped sulfur vacancy-rich MoS₂ (P-M-1) exhibited an excellent electrocatalytic N₂-to-NH₃ conversion efficiency under ambient conditions with a large FE of 12.22% and a high NH₃ yield rate of 60.27 $\mu\text{g h}^{-1} \text{mg}^{-1}_{\text{cat.}}$, outperforming its counterpart of C-MoS₂ (6.02% and 20.31 $\mu\text{g h}^{-1} \text{mg}^{-1}_{\text{cat.}}$) and most of reported aqueous-based NRR electrocatalysts. Further mechanism study revealed that SVs induced by P atoms served as the active sites to adsorb N₂ molecules. Moreover, P dopants also modulated the electronic structure of MoS₂, which facilitated the adsorption of N₂ molecules and further promoted the catalytic activity towards NRR.

* Corresponding authors at: School of Materials Science and Engineering, Central South University, Changsha 410083, China.

E-mail addresses: wanglb@csu.edu.cn (L. Wang), zwu2012@csu.edu.cn (Z. Wu).

2. Experimental section

2.1. Fabrication of C-MoS₂ and P-doped sulfur vacancy-rich MoS₂ catalysts

Firstly, 0.726 g Na₂MoO₄•2H₂O was dissolved into 40 mL deionized water, and then 1.13 g CH₃CH₂NS and 0.318 g NaH₂PO₂•H₂O were successively added into the solution under stirring for 10 min. After being stirred to form a transparent solution, 0.75 mL concentrated HCl was dropped into the solution and continuously stirred for 30 min. Next, the solution was transferred into a 100-mL Teflon-lined stainless-steel autoclave and maintained at 200 °C for 24 h. After being naturally cooled to room temperature, the as-prepared samples were obtained by centrifugation, primarily washed in 0.1 M HCl thrice to remove NH₄⁺ completely, and then washed by absolute ethanol and ultrapure water for several times, and dried at 80 °C overnight, which was marked as P-M-1. Analogously, common MoS₂ without P incorporation and other P-doped MoS₂ samples were also synthesized following a similar process with different contents of NaH₂PO₂•H₂O (0 g, 0.159 g, 0.636 g, 1.272 g), which were successively named as C-MoS₂, P-M-0.5, P-M-2, and P-M-4, respectively. Moreover, for comparison, P-M-1 was annealed at 400 °C for 2 h in Ar and marked as A-P-M-1.

2.2. Preparation of working electrodes

The catalyst powder (3 mg) was dispersed in a mixture of 720 μL water, 200 μL ethanol, and 80 μL of 5 wt% Nafion and then sonicated for 30 min. Next, 5 μL of the catalyst ink was introduced dropwise onto a well-polished GCE surface (d = 3 mm) and dried at room temperature.

2.3. Characterization

The X-ray diffraction (XRD) patterns were obtained using a D/max-2500 X-ray Diffractometer with a Cu K α radiation ($\lambda = 0.154$ nm). The scanning electron microscopy (SEM) images were collected on a FEI Sirion 200 scanning electron microscope. The transmission electron microscopy (TEM) images and high-resolution TEM (HRTEM) images were recorded on a JEOL-2100F transmission electron microscope. The X-ray photoelectron spectroscopy (XPS) measurements were performed on a ESCALAB 250 Xi using Al K α as the exciting source. The binding energy value of each element was calibrated using C 1s = 284.6 eV. The Raman spectra were acquired using the LabRAMHR-800 of French company HORIBA at 633 nm.

2.4. Electrochemical measurements

Before NRR tests, the Nafion membrane was pre-treated by heating in 5% H₂O₂ solution and ultrapure water at 80 °C for 1 h, respectively. Electrochemical NRR measurements were performed in a two-compartment cell separated by Nafion 211 membrane using a CHI 660E electrochemical analyzer (CHI Instruments, Inc., Shanghai). The electrochemical experiments were carried out with a three-electrode configuration using a platinum sheet as the counter electrode and Ag/AgCl electrode (saturated KCl) as the reference electrode. The working electrodes were the modified GCEs with various catalysts. Potentials reported in this work were converted to RHE scale via calibration with the following equation: E(vs. RHE) = E(vs. Ag/AgCl) + 0.197 + 0.059 × pH. All presented current density values were normalized to the geometric surface area. Prior to the electrochemical experiments, the electrolyte solution was poured into high purity Ar gas to remove any residual gas. Linear sweep voltammetry (LSV) was conducted in an Ar- and N₂-saturated 0.1 M Na₂SO₄ solution at a scan rate of 2 mV s⁻¹ to obtain the polarization curves. The electrochemical impedance spectroscopy (EIS) was also tested in the frequency range from 10⁰ Hz to 10⁶ Hz in an N₂-saturated 0.1 M Na₂SO₄ solution. Each collected aliquot was titrated three times by the indophenol blue method to measure the NH₃

concentration, thus the FE and their yield rate. Before NRR experiments, the 0.1 M Na₂SO₄ electrolyte was pre-saturated with the N₂ gas for 30 min. All experiments were carried out at room temperature.

For more details, please see the [Appendix A Supplementary data](#).

3. Results and discussion

3.1. Characterization of the samples

To begin with, common MoS₂ (C-MoS₂) with a spherical structure was fabricated via a hydrothermal method ([Figs. S1 and S2](#)). High-resolution transmission electron microscopy (HRTEM) image of C-MoS₂ ([Fig. 1a](#)) illustrated the typical lamellar structure with a lattice fringe distance of 0.62 nm relating to the (002) planes of crystalline MoS₂ [\[22–24\]](#). The synthesis of P-doped MoS₂ catalysts underwent similar procedures except for additionally adding NaH₂PO₂•H₂O as the P source. A series of P-doped MoS₂ catalysts were obtained according to the amount of added NaH₂PO₂•H₂O, named P-M-0.5, P-M-1, P-M-2, and P-M-4, respectively. Besides, P-M-1 annealed at 400 °C under argon (Ar) atmosphere (denoted as A-P-M-1) was also prepared for further comparison. [Fig. S3](#) displayed the X-ray diffraction (XRD) patterns of the as-obtained catalysts. The diffraction peaks at 14.0°, 32.8°, and 56.9° of C-MoS₂ corresponded to (002), (100), and (110) planes of the standard MoS₂ (JCPDS no. 75-1539), respectively [\[20–22\]](#). These diffraction peaks gradually weakened from P-M-0.5 to P-M-2 and almost disappeared in P-M-4, indicating that the introduction of P dopants evidently receded the crystallinity of the catalysts. After annealing P-M-1, the diffraction peaks of (110) and (100) planes became sharper again and the peak for (002) planes was obviously observed for A-P-M-1. The formation of MoS₂ in amorphous states in P-M-1 was further proved by Raman spectra measurements ([Fig. S4](#)). As depicted in the scanning electron microscopy (SEM) and transmission electron microscopy (TEM) images of P-M-1, the spherical structure with an average size of about 100 nm was maintained, which was beneficial for exposing additional edge catalytic sites ([Fig. 1b and c](#)). Further observations in the HRTEM image of P-M-1 ([Fig. 1d](#)) showed abundant disordered structures as well as distortions and kinks in the slabs of MoS₂ due to the disorder within the basal planes of the nanosheets as previously observed in the literature [\[25,26\]](#). Besides, the atom arrangements in the basal planes of P-M-1 further exhibited a high density of defects identified as slightly brighter spots in the position of sulfur atoms ([Fig. 1e](#)). Notably, the SVs in P-M-1 preferred to be linear distributed with a general number of 3–4 and extended in another direction to form an in-plane defect cluster. On the contrary, A-P-M-1 possessed typical lamellar structures with well-organized atom configuration and reduced defects in the basal planes ([Fig. 1g and f](#)). Meanwhile, the diffraction patterns of the HRTEM images for C-MoS₂, P-M-1, and A-P-M-1 (the inset of [Fig. 1a, d, f](#)) also proved the transition from the amorphous phase to crystal, which was consistent with the XRD results. Moreover, energy-dispersive X-ray (EDX) elemental mapping of P-M-1 was also conducted, demonstrating a homogeneous distribution of Mo, S, and P elements ([Fig. 1h–k](#)). Based on inductively coupled plasma atomic emission spectra (ICP-AES) results, the S/Mo ratio of C-MoS₂ was close to 2 as expected, while the S/Mo ratio reduced after the incorporation of P, manifesting that the P-doping removed a portion of S atoms from the MoS₂ basal plane to form SVs ([Table S1](#)). Besides, Brunauer-Emmett-Teller (BET) surface areas of C-MoS₂, P-M-0.5, P-M-1, P-M-2, P-M-4, and A-P-M-1 were determined to be 16.96, 72.62, 90.14, 32.04, 15.33, and 13.81 m² g⁻¹, respectively ([Table S2](#)). One can see that the BET surface area value was gradually enlarged with the increased contents of P dopants and achieved the maximum over P-M-1, then dropped down, which should be attributed to the aggregations of particles induced by excess doping of P, as demonstrated by the SEM image in [Fig. S5](#).

X-ray photoelectron spectroscopy (XPS) was measured to elucidate the chemical states of the obtained catalysts. The survey of P-M-1 demonstrated the presence of Mo, S, and P elements ([Fig. S6](#)). As shown

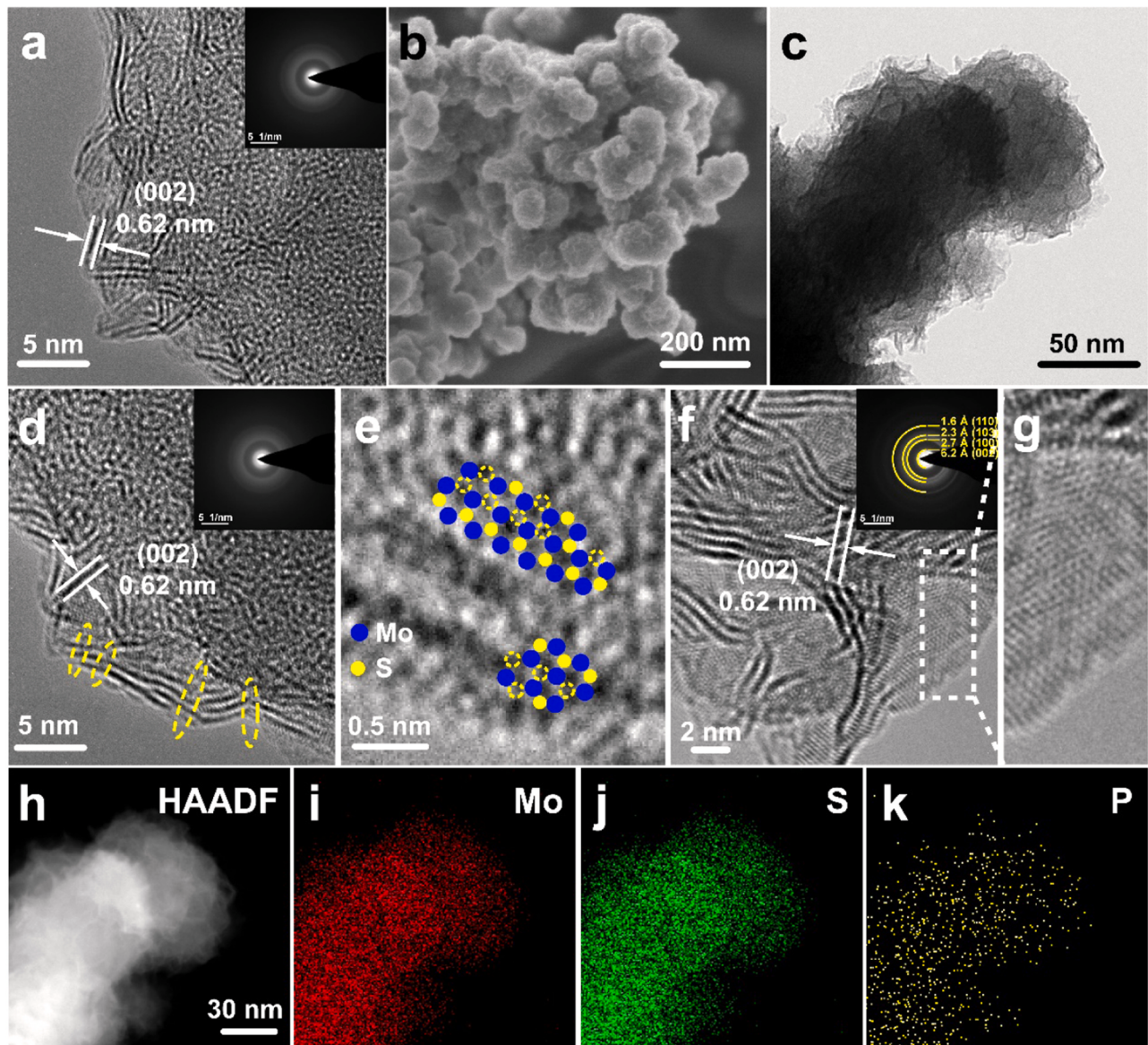


Fig. 1. HRTEM images of (a) C-MoS₂. (b) SEM and (c) TEM image of P-M-1. HRTEM images of (d–e) P-M-1 and (f) A-P-M-1. (g) The image of the region enclosed by the white rectangle of panel f. (h–k) EDX mapping images of P-M-1. The inset images in panel (a), (d), and (f) were the corresponding FFT patterns.

in Mo 3d spectra of C-MoS₂ (Fig. 2a), the binding energies (BEs) of Mo 3d_{5/2} and 3d_{3/2} were about 229.5 and 232.7 eV, respectively, corresponding to the Mo⁴⁺ states [27]. The peaks centered at 228.5 and 231.7 eV were originated from the undercoordinated molybdenum (Mo (UC)) due to the presence of SVs [28]. In the P-doped MoS₂, the XPS peaks shift to low energies due to the incorporation of P atoms, which have a lower electronegativity than the host S atoms [29], implying that P-doping can tailor the electronic structure of neighbor Mo atoms. The doublets at 229.4 and 232.6 eV can be attributed to the Mo⁴⁺ states of MoS₂ [30], and signals detected at 228.4 and 231.6 eV pertain to Mo (UC). Binding energies centered at 228.9 and 232.0 eV, respectively, are related to the Mo 3d_{5/2} and Mo 3d_{3/2} orbitals of Mo bonded to P heteroatoms (P-Mo) [31]. Based on the integral area, the content of Mo(UC) was enlarged with the increase of P dopants, further proving that the formation of SVs was triggered by the incorporation of P. Fig. 2b displayed the S 2p spectra of the obtained catalysts. For C-MoS₂, the BEs at 162.4 and 163.5 eV corresponded to terminal S₁²⁻ species of crystalline phase, while the doublets at 163.7 and 165.0 eV were ascribed to bridging S₂²⁻ species of amorphous MoS_x [32]. These peaks of S anions in P-doped MoS₂ catalysts shifted slightly towards the lower binding

energy direction, indicative of the electron transfer from P to S anions [33]. Additionally, the P 2p XPS spectrum for P-M-1 (Fig. 2c) displayed P 2p_{3/2} and P 2p_{1/2} doublet peaks located at respective 130.1 and 130.8 eV, demonstrating the successful doping of P into the MoS₂ matrix [31]. We further calculated the contents of bridging S₂²⁻ species in the obtained catalysts based on the XPS data. As shown in Fig. 2d, the concentration of bridging S₂²⁻ species gradually elevated with the increased amount of P dopants, while sharply decreased for A-P-M-1, implying that some SVs were repaired during the calcination process. Thus, it was speculated that partial S sites were occupied by P atoms during the doping and then bridged with the neighbor S atoms to form SVs and bridging S₂²⁻ species, which reverted to the initial sites to pursue a stable state after calcination.

Furthermore, electron paramagnetic resonance (EPR) was performed in order to estimate the concentration evolution of SVs in the obtained catalysts. As depicted in Fig. 2e, the signature of the Mo–S dangling bonds was detected at $g = 2.003$ for all the catalysts. The EPR signals in C-MoS₂ were originated from the defects as expected for solution-processed materials [28]. Generally, the intensity of the EPR signal is proportional to the concentration of dangling bonds from the SVs in the

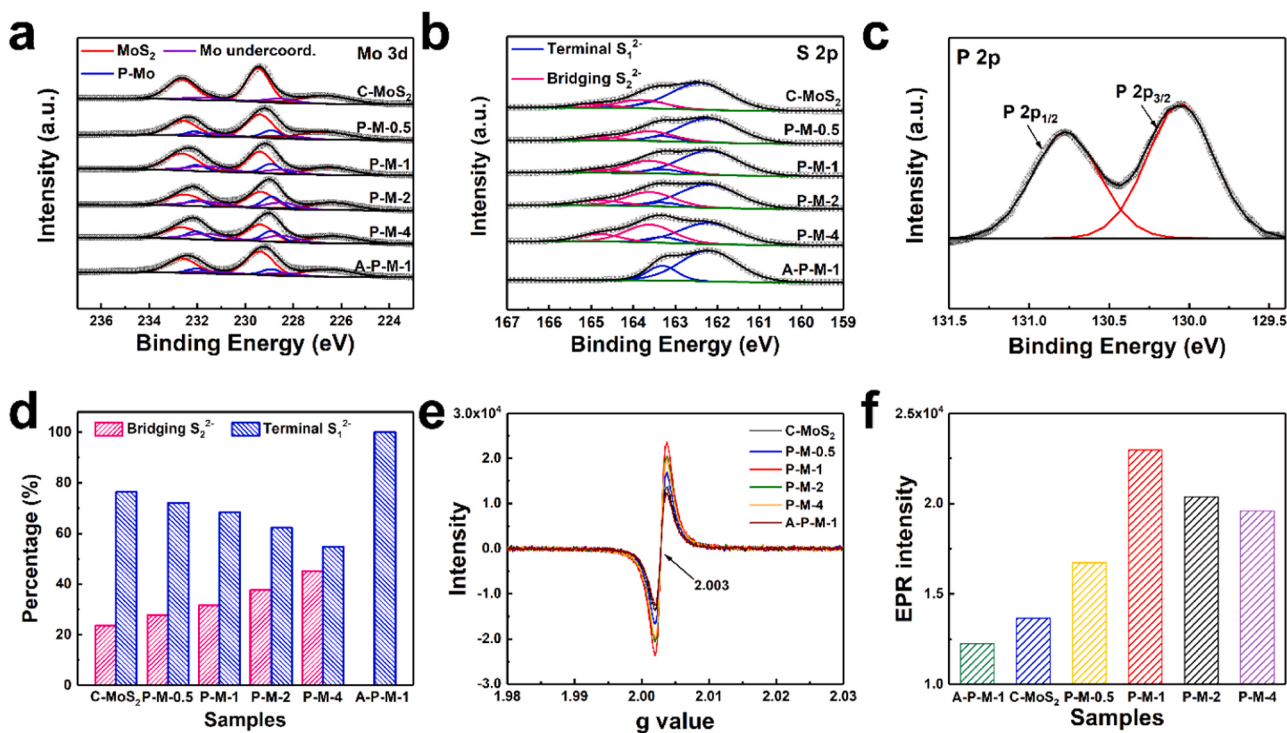


Fig. 2. XPS spectra in the (a) Mo 3d and (b) S 2p regions for all samples. (c) XPS spectra in the P 2p regions for P-M-1. (d) Relative fractions of bridging S₂²⁻ and terminal S₁²⁻ in all samples. (e) EPR spectra generated by the Mo-S dangling bonds for the different MoS₂ samples. (f) Evolution of the intensity of the EPR signals as a function of the P doping.

MoS₂ slabs. In terms of the EPR signal strength, the signal was gradually enhanced with the increase of doped P atoms and peaked at P-M-1, whereas further doping P atoms in MoS₂ lowered the EPR signal, which was probably attributed to the nature of defects (Fig. 2f). Before P-M-1, “point” defects were created and generated Mo-S dangling bonds

responsible for the EPR signals. Beyond P-M-1, S atoms got stripped heavily when introducing more P atoms, leading to the formation of vastly elongational defects and further the decrease of the quantity of Mo-S dangling bonds in the MoS₂ slab (Fig. S7). In addition, the dramatically shrinking EPR signal of A-P-M-1 compared with that of

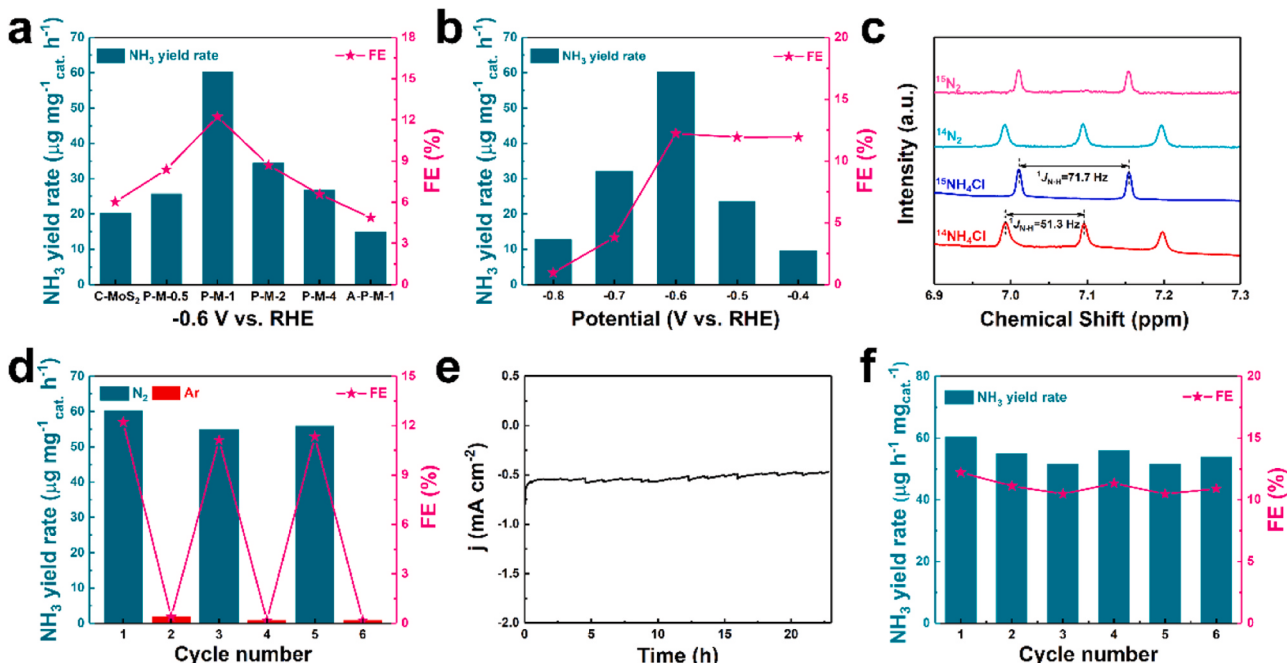


Fig. 3. (a) Comparison of properties (NH₃ yield rates and FEs) at -0.6 V vs. RHE for various catalysts under the same conditions. (b) The properties of P-M-1 at various potentials. (c) ¹H-NMR (500 MHz) spectra of solution after electrocatalytic N₂ fixation using P-M-1 in ¹⁴N₂ or ¹⁵N₂ atmosphere. (d) NH₃ yield rates and corresponding FEs of P-M-1 with switching 2 h cycles between N₂- and Ar-saturated electrolytes. (e) Time-dependent current density curve of P-M-1 at -0.6 V for 23 h. (f) Stability test of P-M-1 during repeated NRR at -0.6 V.

P-M-1 manifested the decrease of SVs after annealing, which was in agreement with the XPS results. Based on the above analysis, we successfully constructed and regulated SVs in MoS₂ by simply introducing P dopants.

3.2. NRR performance of the samples

The catalytic performance of the as-obtained catalysts was evaluated toward electrocatalytic N₂ reduction by spectrophotometrically measuring the generated NH₃ via indophenol blue method (Fig. S8) [34]. The catalysts were dropped onto glassy carbon electrodes and tested as NRR working electrodes under ambient conditions in an electrolytic cell separated by a Nafion membrane. During the N₂ electrolysis, N₂ was supplied onto the cathode, and the H⁺ in the electrolytic cell was transferred through the Na₂SO₄ electrolyte to react with N₂ to generate NH₃. All potentials were reported vs. RHE. Fig. 3a showed the NH₃ yield rates and FEs of as-obtained catalysts at the potential of -0.6 V. The NH₃ production rates were 20.31, 25.71, 60.27, 34.35, 26.79, and 14.91 $\mu\text{g h}^{-1} \text{mg}^{-1}_{\text{cat}}$ for C-MoS₂, P-M-0.5, P-M-1, P-M-2, P-M-4, and A-P-M-1, respectively (Fig. 3a, b, and S9–S11). Besides, P-M-1 also exhibited the highest FE of 12.22%, which was 2.03, 1.49, 1.40, 1.86, and 2.51 times higher than that of C-MoS₂, P-M-0.5, P-M-2, P-M-4, and A-P-M-1, respectively (Fig. 3a and b). The linear sweep voltammetry (LSV) curves of P-M-1 in N₂- and Ar-saturated 0.1 M Na₂SO₄ electrolytes were depicted in Fig. S12. It was clearly seen that P-M-1 exhibited a higher catalytic current density in the N₂-saturated solution, demonstrating the activity of electrocatalytic N₂ reduction [35,36]. It was worth mentioning that both the NH₃ yield rate and FE of P-M-1 were significantly reduced when the applied potential exceeded -0.6 V, probably ascribed to the gradually enhanced competitive hydrogen evolution reaction (HER) (Fig. 3b) [37–39]. To double-check the production of NH₃, we also employed Nessler's reagent method to determine the production rate of NH₃. The comparable results confirmed the reliability of the ammonia detection by the indophenol blue method (Figs. S13 and S14). Thus, P-M-1 possessed the highest catalytic activity towards electrocatalytic N₂ reduction, superior to that of most Mo-based NRR electrocatalysts operating under ambient conditions reported to date, including MoS₂ nanosheets (13.09 $\mu\text{g h}^{-1} \text{mg}^{-1}_{\text{cat}}$, 1.17%) [19], defect-rich MoS₂ nanoflowers (29.28 $\mu\text{g h}^{-1} \text{mg}^{-1}_{\text{cat}}$, 8.34%) [20], MoS₂-rGO (24.82 $\mu\text{g h}^{-1} \text{mg}^{-1}_{\text{cat}}$, 4.58%) [21], MoO₃ nanosheets (29.43 $\mu\text{g h}^{-1} \text{mg}^{-1}_{\text{cat}}$, 1.9%) [40], and many other aqueous-based NRR electrocatalysts, such as Au/TiO₂ (21.4 $\mu\text{g h}^{-1} \text{mg}^{-1}_{\text{cat}}$, 8.11%) [41], PCN (8.09 $\mu\text{g h}^{-1} \text{mg}^{-1}_{\text{cat}}$, 11.59%) [42], FeN₄ (10.25 $\mu\text{g h}^{-1} \text{mg}^{-1}_{\text{cat}}$, 10.5%) [43], etc. A more detailed comparison is listed in Table S3. Moreover, we also tested the NRR properties of P-M-1 in 0.1 M HCl and 0.1 M KOH solution (Fig. S15). The NH₃ yield rates and FEs in these electrolytes were lower than that in the neutral electrolyte, which might be attributed to the immensely enhanced competitive HER.

To further verify that the product was indeed generated via the N₂ reduction electro-catalyzed by P-M-1, an isotopic labeling study by using ¹⁵N₂ as the purging gas was designed. The obtained ¹⁵NH₄⁺ was measured by ¹H nuclear magnetic resonance (NMR) spectroscopy. As shown in ¹H NMR spectra (Fig. 3c), the isotopically labeled sample exhibited the doublets of ¹⁵NH₄⁺, reaffirming that the generated ammonia indeed originated from N₂ fixation. Then we further operated the ¹⁵N isotope labeling experiments which were quantified as recommended by Anderson et al. [44–46]. As shown in Fig. S16, the produced ¹⁵NH₄⁺ in the electrochemical reaction over P-M-1 for 1 h and 2 h by feeding ¹⁵N₂ were a diploid relationship, in which the produced ¹⁵NH₄⁺ for 2 h was also consistent with that by feeding ¹⁴N₂ (Figs. 3b and S16d), indicating that the N in the generated NH₄⁺ was indeed from the N₂ supply rather than other nitrogenous pollutants. In addition, we used IC to examine the nitrogen oxides (NO_x) in the electrolyte or derived from the feeding gas (Fig. S17). One can see that there were only 0.003 and 0.002 $\mu\text{g mL}^{-1}$ NO₂⁻ and NO₃⁻ producing NH₄⁺ through NRR, thus the NH₃ yield rate of NO_x transformation was 1.67 $\mu\text{g h}^{-1} \text{mg}^{-1}_{\text{cat}}$, which

was much lower than that of 60.27 $\mu\text{g h}^{-1} \text{mg}^{-1}_{\text{cat}}$, indicating that the NH₄⁺ produced in our system cannot come from those nitrogen oxide pollutants. Furthermore, we tested the NRR performance over P-M-1 in the electrolyte and the feeding N₂ was pre-treated using 0.5 M H₂SO₄. There was a negligible difference between Figs. S18 and 3b, further demonstrating that almost no nitrogen oxide pollutants can be found in the generated NH₄⁺. What's more, almost no NH₃ was detected when the N₂ reduction reaction was conducted at open-circuit potential (OCP), in an Ar-saturated 0.1 M Na₂SO₄ solution, or without catalysts (blank GCE) (Fig. S19). Besides, when the reaction was catalyzed by P-M-1 at -0.6 V with switching 2 h cycles between N₂- and Ar-saturated 0.1 M Na₂SO₄ solution, the generation of NH₃ was only obtained in N₂-saturated solution at -0.6 V (Fig. 3d). All these results further confirmed that the detected NH₃ only originated from the electro-catalyzed conversion of N₂ over the P-M-1 catalyst. Note that N₂H₄ was not detected after the electrocatalytic reaction at various potentials, suggesting the excellent selectivity of P-M-1 for NH₃ production (Figs. S20 and S21).

Durability is also a critical parameter to evaluate the catalytic performances [47–50]. The time-dependent current density curve for P-M-1 at -0.6 V in the N₂-saturated 0.1 M Na₂SO₄ was presented in Fig. 3e. After the NRR electrolysis for 23 h, P-M-1 still maintained a good long-term electrochemical stability with only a small attenuation in the current density. Additionally, catalytic tests with reaction time prolonging to 8 h were conducted for P-M-1, where the amount of produced NH₃ was linearly increased with reaction time (Fig. S22). The durability of P-M-1 was further studied by carrying out successive reaction rounds. As revealed in Fig. 3f, both NH₃ yield and FE showed small variations after six consecutive cycles, indicating the remarkable durability of P-M-1. Moreover, P-M-1 catalyst residue after reacting for 23 h (named as P-M-1-used) was further characterized by a series of techniques. The XRD analysis validated the preserved MoS₂ nature (Fig. S23). TEM and HRTEM images of P-M-1-used showed that the morphology features and defects in P-M-1 were well-maintained after the long-term NRR electrolysis (Fig. S24). In addition, XPS spectra solidly proved that there was a negligible change in the concentration of dangling bonds from the SVs in P-M-1 before and after NRR electrolysis (Fig. S25). Moreover, the pH value of the Na₂SO₄ aqueous solution before and after electrocatalytic NRR hardly changed significantly, as shown in Fig. S26. As a result, P-M-1 catalyst exhibited extraordinarily catalytic activity, selectivity, and stability towards NRR.

3.3. Activity enhancement mechanism of P-M-1

We further explored the mechanism of the superior catalytic performance of P-M-1 towards electrocatalytic NRR in detail. Nitrogen temperature-programmed desorption (N₂-TPD) was conducted to investigate the nitrogen adsorptive capacity of various catalysts. As plotted in Fig. S27, the desorption peaks at 200–350 °C were assigned to the chemisorption of N₂ [51]. The nitrogen adsorptive capacity of P-M-1 was much higher than that of other catalysts, indicating a promoted adsorption of N₂ as well as a better mass transportation ability in the NRR. Besides, the annealed A-P-M-1 with the absence of SVs possessed the weakest signal. Moreover, electrochemical active surface area (ECSA) was measured for the as-obtained catalysts to evaluate the number of activity sites (Fig. 4a and S28; Table S4) [52–54]. P-M-1 possessed the largest ECSA value of 5.96 cm^2 among all the catalysts, thus providing more active sites for the N₂ reduction process. The sharply decrease ECSA value for A-P-M-1 was ascribed to the reduction of SVs during calcination, as revealed in Fig. 2a and f. Fig. 4b depicted the evolution of the NH₃ yield rates with the values of ECSA (positively related to the number of SVs), further demonstrating the dependence of NRR properties on SVs. Consequently, SVs in P-M-1 were considered as the active sites to efficiently absorb N₂ molecules for further hydrogenation to NH₃. Furthermore, electrochemical impedance spectroscopy (EIS) was also collected to investigate the electron transfer efficiency

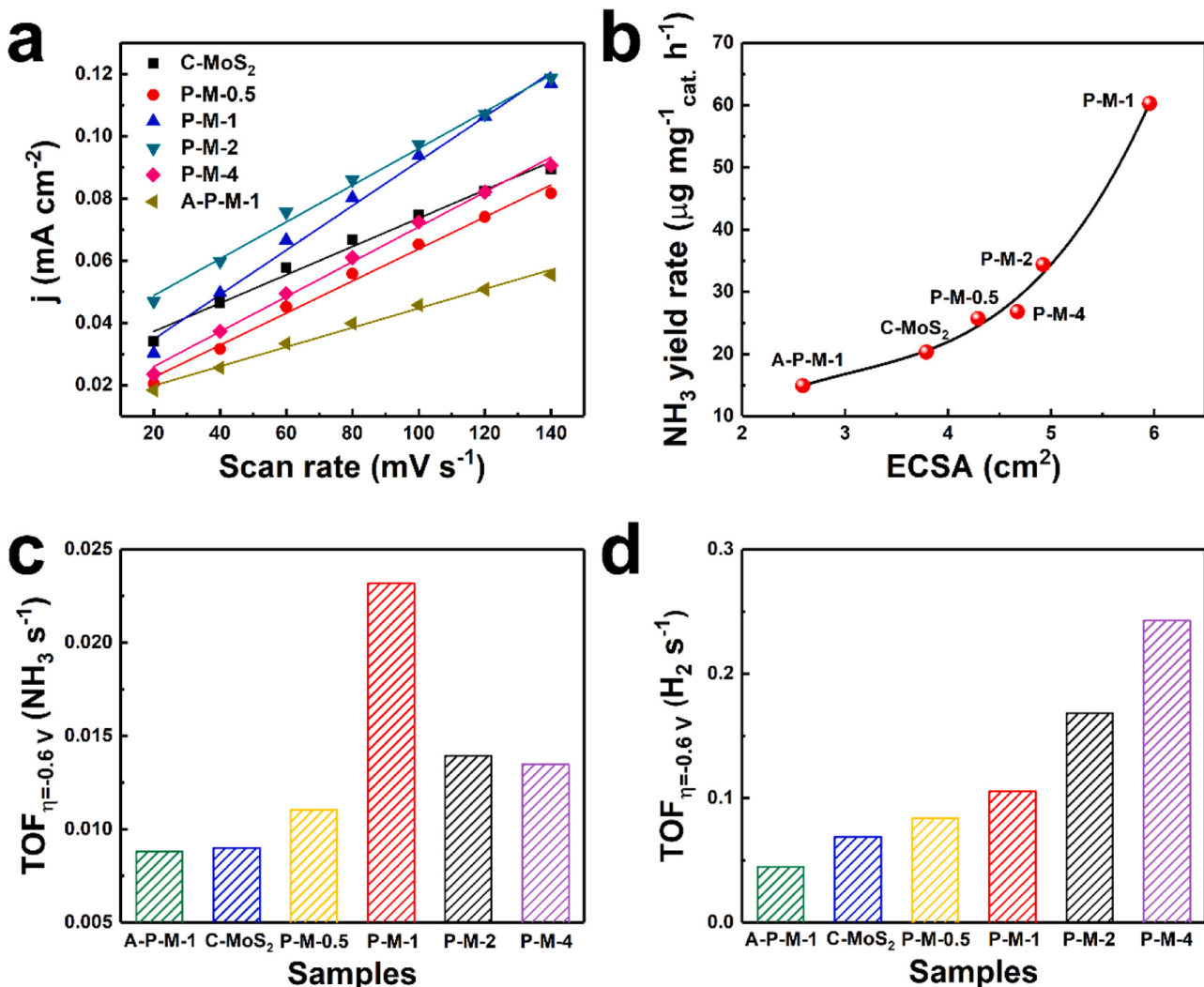


Fig. 4. (a) Measured capacitive currents plotted as a function of scan rate. (b) Evolution of the NH₃ yield rates with the value of ECSA. Evolution of the (c) TOF_{NRR} and (d) TOF_{HER} measured at -0.6 V for all samples.

during N₂ reduction. As illustrated in the corresponding Nyquist plots in Fig. S29, P-M-1 exhibited the minimum values of charge transfer resistance, indicating a better electron transferability as well as more facile electrode kinetics for the improved NRR performance. The higher charge transfer resistance for P-M-2 and P-M-4 may be attributed to the aggregations of particles induced by excess doping of P (Fig. S5). The larger particle size of P-M-2 and P-M-4 and severe aggregations increased the diffusion length of electrons from catalysts to redox couples in the electrolyte, thus resulting in a larger charge transfer resistance and inferior catalytic activity towards NRR [32,55].

Considering the competitive relation of NRR and HER together, HER performances in Ar-saturated 0.1 M Na₂SO₄ solution were also drawn to understand the evolution of activities in essence. Turnover frequency (TOF) tests for NRR (TOF_{NRR}) and HER (TOF_{HER}) were measured to evaluate the intrinsic activity of the as-obtained catalysts (Figs. 4c, d, and S30). As displayed in Fig. 4c, TOF_{NRR} detected at -0.6 V was promoted with the increase of P dopants and reached maximum at P-M-1, while excessive P doping diminished TOF_{NRR}. Similar to that of the contents of SVs in the catalysts, this variation trend of TOF_{NRR} implied that SVs were in favor of NRR, corresponding to the previous literature [56–58], which was in line with TPD and ECSA results above. On the contrary, the HER performance of obtained catalysts (Fig. S30a) gradually enhanced with the increase of P dopants from C-MoS₂ to P-M-4, in accordance with TOF_{HER} (Fig. 4d and S30b). The evolution of TOF_{HER}

with the content of bridging S₂²⁻ (Fig. S31) suggested the active role of the bridging S₂²⁻ in HER [22,57,59]. Thus, we speculated that NRR preferred to occur on SVs sites while bridging S₂²⁻ species serve as active sites for competitive HER (Fig. S32).

3.4. DFT calculations

To further investigate the catalytic mechanism of the NRR process at the site of SVs, density functional theoretical (DFT) calculations were also performed. Three models were developed: P-doped MoS₂ with and without SVs (P-SV-MoS₂ and P-MoS₂) and SV-MoS₂ without P doping (SV-MoS₂) (Fig. S33). The adsorption of N₂ molecules over different models was first considered. As observed in Fig. 5a, P-MoS₂ was barely able to adsorb N₂ molecules due to the high N₂ adsorption energy of 1.68 eV. As for SV-MoS₂, the adsorption of N₂ molecule significantly reduced to 0.38 eV, declaring that SVs near Mo atoms were capable of efficiently adsorbing N₂ molecules and further promoting the catalytic activity of the basal plane of MoS₂. Nevertheless, three Mo atoms, interacting with N₂ by donating electrons to nitrogen's antibonding orbital, significantly increases the free energy, thus hindering the N₂ adsorption rate [57]. After the doping of P atoms, electrons tended to accumulate around Mo atoms adjacent to the doped P atoms from the isosurfaces of deformation charge density (Fig. 5b), resulting in much lower adsorption energy of N₂ molecules (-0.21 eV) over P-SV-MoS₂.

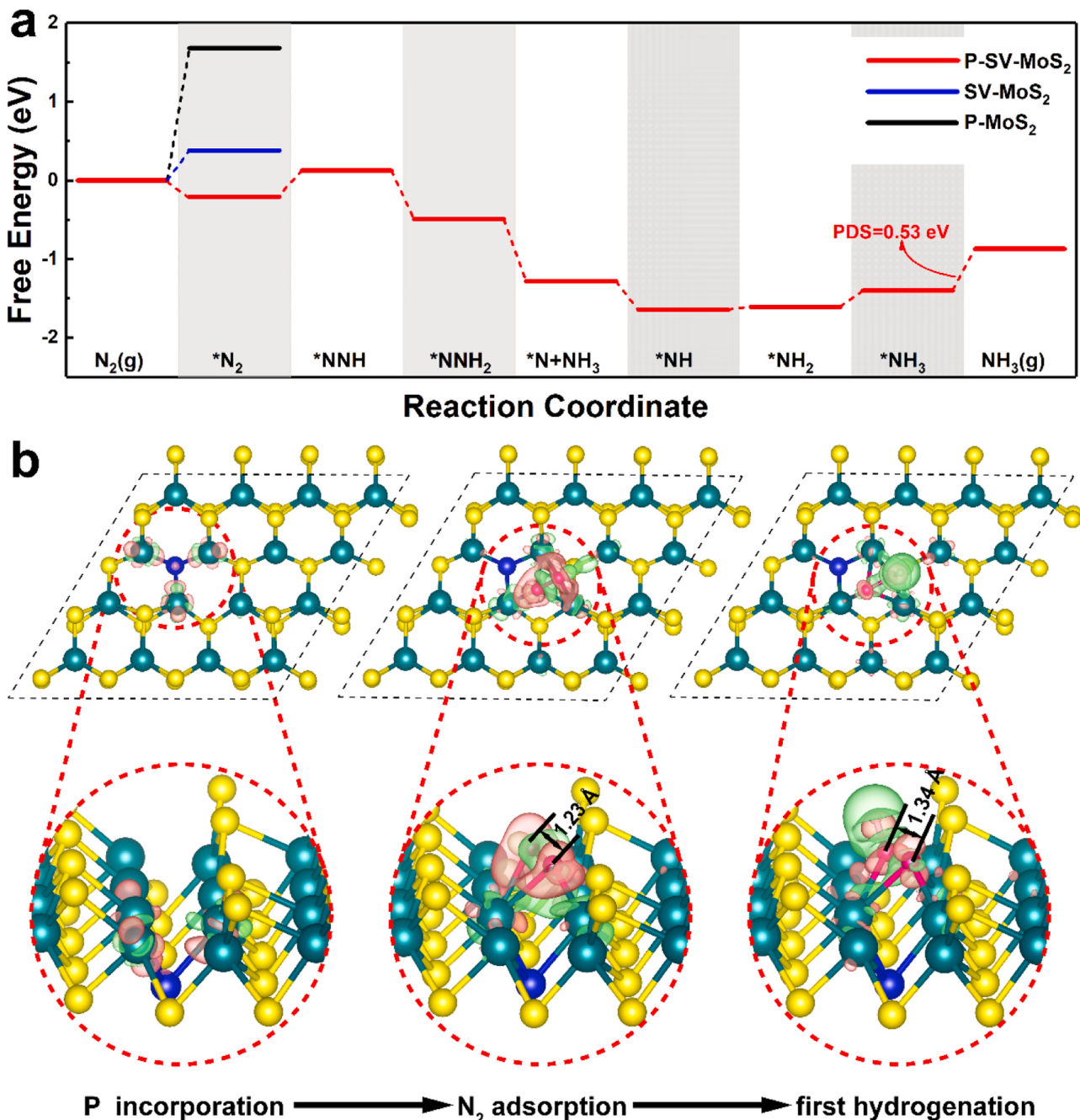


Fig. 5. (a) Calculated pathway for NRR over P-SV-MoS₂, P-MoS₂, and SV-MoS₂. The adsorption site was denoted by an asterisk (*). (b) Charge density difference of P incorporation, N₂ adsorption and the first hydrogenation step over P-SV-MoS₂, respectively. Electron excess and deficiency were represented as red and green isosurfaces, respectively.

(denoted as $\text{N}_2^*-\text{P-SV-MoS}_2$). As a result, the introduction of P atoms not only induced SVs in MoS₂, but also modulated the electronic structure of MoS₂, further facilitating the adsorption of N₂ molecules on the surface of P-SV-MoS₂. In addition, we also compared the nitrogen adsorption energy of different samples, as shown in Fig. S34. One can see that the nitrogen adsorption energy became more negative with the increase of P dopants, indicating the active role of P incorporation in NRR. Moreover, the pathways for the NRR process over P-SV-MoS₂ were investigated. When introducing one H atom to $\text{N}_2^*-\text{P-SV-MoS}_2$, the depletion of electrons occurred in the region between the two N atoms while electrons accumulated around the N-Mo and N-H bonds, indicating the charge transfer from N₂ molecule to Mo atoms edge (Fig. 5b). In this step, the N-N bond length was significantly elongated from 1.23 Å in

$^*\text{N}_2$ to 1.34 Å in $^*\text{NNH}$ with an energy change of 0.33 eV, thus promoting the subsequent hydrogenation step [60]. As shown in Fig. S35, further hydrogenation of N₂ favored distal pathway over P-SV-MoS₂, where the desorption of the second NH₃ molecule ($^*\text{NH}_3$ to NH₃) was a potential-determining step with an energy barrier of 0.53 eV. Notably, the generated NH₃ was easily dissolved in the reaction solution, contributing to the release of NH₃ and the regeneration of active centers for long-term N₂ reduction.

4. Conclusions

In summary, P-doped sulfur vacancy-rich MoS₂ was successfully fabricated by a facile hydrothermal route and was verified as a highly

efficient non-noble metal catalyst to enable the electro-hydrogenation of N_2 for the NH_3 production under ambient conditions. The optimized P-M-1 catalyst achieved a high NH_3 yield rate of $60.27 \mu\text{g h}^{-1} \text{mg}^{-1}_{\text{cat}}$, and a large FE of 12.22% at -0.6 V vs. RHE in $0.1 \text{ M Na}_2\text{SO}_4$. From both experimental and theoretical perspectives, the doping of P atoms created rich SVs in MoS_2 , which served as active sites for the adsorption and transformation of N_2 molecules. Moreover, P dopants regulated the electronic structures of MoS_2 by facilitating the interfacial electron transfer from catalysts to adsorbed N_2 molecules with smaller resistance, responsible for the remarkable catalytic performance of P-M-1. This work not only fabricated a high-performance P-doped MoS_2 catalyst for NRR, but also proved that defect engineering was an effective strategy to improve the catalytic performance that was worth being applied to other catalytical reactions.

CRediT authorship contribution statement

Hao Fei: Conceptualization, Methodology, Writing – original draft. **Ting Guo:** Data curation, Software. **Yue Xin:** Writing – review & editing. **Liangbin Wang:** Data curation, Software. **Ruoqi Liu:** Validation, Investigation. **Dezhi Wang:** Formal analysis. **Fangyang Liu:** Visualization, Investigation. **Zhuangzhi Wu:** Supervision, Writing – review & editing.

Declaration of Competing Interest

The authors declare that they have no known competing financial interests or personal relationships that could have appeared to influence the work reported in this paper.

Acknowledgment

Financial supports from the Natural Science Foundation of Hunan Province of China (Grants 2020JJ4730, 2018RS3019 and 2019JJ30033) are gratefully acknowledged.

Appendix A. Supplementary material

Supplementary data associated with this article can be found in the online version at [doi:10.1016/j.apcatb.2021.120733](https://doi.org/10.1016/j.apcatb.2021.120733).

References

- [1] V. Smil, Detonator of the population explosion, *Nature* 400 (1999) 415.
- [2] R.W. Howarth, Coastal nitrogen pollution: a review of sources and trends globally and regionally, *Harmful Algae* 8 (2008) 14–20.
- [3] V. Rosca, M. Duca, M.T. de Groot, M.T.M. Koper, Nitrogen cycle electrocatalysis, *Chem. Rev.* 109 (2009) 2209–2244.
- [4] C. Guo, J. Ran, A. Vasileff, S.Z. Qiao, Rational design of electrocatalysts and photo (electro) catalysts for nitrogen reduction to ammonia (NH_3) under ambient conditions, *Energy Environ. Sci.* 11 (2018) 45–56.
- [5] K.C. KMacLeod, P.L. Holland, Recent developments in the homogeneous reduction of dinitrogen by molybdenum and iron, *Nat. Chem.* 5 (2013) 559–565.
- [6] C.J.M. van der Ham, M.T.M. Koper, D.G.H. Hettterscheid, Challenges in reduction of dinitrogen by proton and electron transfer, *Chem. Soc. Rev.* 43 (2014) 5183–5191.
- [7] Q.C. Wang, Y.P. Lei, D.S. Wang, Y.D. Li, Defect engineering in earth-abundant electrocatalysts for CO_2 and N_2 reduction, *Energy Environ. Sci.* 12 (2019) 1730–1750.
- [8] T. Xu, B.Y. Ma, J. Liang, L.C. Yue, Q. Liu, T.S. Li, H.T. Zhao, Y.L. Luo, S.Y. Lu, X. P. Sun, Recent progress in metal-free electrocatalysts toward ambient N_2 reduction reaction, *Acta Phys. Chim. Sin.* 37 (2021), 2009043.
- [9] B.Y. Ma, H.T. Zhao, T.S. Li, Q. Liu, Y.S. Luo, C.B. Li, S.Y. Lu, A.M. Asiri, D.W. Ma, X. P. Sun, Iron-group electrocatalysts for ambient nitrogen reduction reaction in aqueous media, *Nano Res.* 14 (2021) 555–569.
- [10] C.C. Lee, Y. Hu, M.W. Ribbe, ATP-independent formation of hydrocarbons catalyzed by isolated nitrogenase cofactors, *Angew. Chem. Int. Ed.* 51 (2012) 1947–1949.
- [11] T. Spatzal, M. Aksoyoglu, L. Zhang, S.L.A. Andrade, E. Schleicher, S. Weber, D. C. Rees, O. Einsle, Evidence for interstitial carbon in nitrogenase FeMo cofactor, *Science* 334 (2011) 940.
- [12] B.M. Hoffman, D. Lukyanov, Z.Y. Yang, D.R. Dean, L.C. Seefeldt, Mechanism of nitrogen fixation by nitrogenase: the next stage, *Chem. Rev.* 114 (2014) 4041–4062.
- [13] Y. Ohki, K. Uchida, M. Tada, R.E. Cramer, T. Ogura, T. Ohta, N_2 activation on a molybdenum-titanium-sulfur cluster, *Nat. Commun.* 9 (2018) 3200.
- [14] A. Banerjee, B.D. Yuhas, E.A. Margulies, Y. Zhang, Y. Shim, M.R. Wasielewski, M. G. Kanatzidis, Photochemical nitrogen conversion to ammonia in ambient conditions with FeMoS -chalcogels, *J. Am. Chem. Soc.* 137 (2015) 2030–2034.
- [15] J. Liu, M.S. Kelley, W. Wu, A. Banerjee, A.P. Douvalis, J. Wu, Y. Zhang, G.C. Schatz, M.G. Kanatzidis, Nitrogenase-mimic iron-containing chalcogels for photochemical reduction of dinitrogen to ammonia, *Proc. Natl. Acad. Sci. USA* 113 (2016) 5530–5535.
- [16] J. Liu, C. Guo, A. Vasileff, S. Qiao, Nanostructured 2D materials: prospective catalysts for electrochemical CO_2 reduction, *Small Methods* 1 (2017) 1–2.
- [17] X. Duan, J. Xu, Z. Wei, J. Ma, S. Guo, H. Liu, S. Dou, Atomically thin transition-metal dichalcogenides for electrocatalysis and energy storage, *Small Methods* 1 (2017), 1700156.
- [18] J. Wang, H. Zhang, X. Wang, Recent methods for the synthesis of noble-metal-free hydrogen-evolution electrocatalysts: from nanoscale to sub-nanoscale, *Small Methods* 1 (2017), 1700118.
- [19] L. Zhang, X. Ji, X. Ren, Y. Ma, X. Shi, Z. Tian, A.M. Asiri, L. Chen, B. Tang, X. Sun, Electrochemical ammonia synthesis via nitrogen reduction reaction on a MoS_2 catalyst: theoretical and experimental studies, *Adv. Mater.* 30 (2018), 1800191.
- [20] X. Li, T. Li, Y. Ma, Q. Wei, W. Qiu, H. Guo, X. Shi, P. Zhang, A.M. Asiri, L. Chen, B. Tang, X. Sun, Boosted electrocatalytic N_2 reduction to NH_3 by defect-rich MoS_2 nanoflower, *Adv. Energy Mater.* 8 (2018), 1801357.
- [21] X. Li, X. Ren, X. Liu, J. Zhao, X. Sun, Y. Zhang, X. Kuang, T. Yan, Q. Wei, D.A. Wu, MoS_2 nanosheet-reduced graphene oxide hybrid: an efficient electrocatalyst for electrocatalytic N_2 reduction to NH_3 under ambient conditions, *J. Mater. Chem. A* 7 (2019) 2524–2528.
- [22] L. Zeng, S. Chen, J. van der Zalm, X. Li, A. Chen, Sulfur vacancy-rich N-doped MoS_2 nanoflowers for highly boosting electrocatalytic N_2 fixation to NH_3 under ambient conditions, *Chem. Commun.* 55 (2019) 7386–7389.
- [23] D. Wang, B. Su, Y. Jiang, L. Li, B.K. Ng, Z. Wu, F. Liu, Polytype 1T/2H MoS_2 heterostructures for efficient photoelectroncatalytic hydrogen evolution, *Chem. Eng. J.* 330 (2017) 102–108.
- [24] D. Yan, H. Li, C. Chen, Y. Zou, S. Wang, Defect engineering strategies for nitrogen reduction under ambient conditions, *Small Methods* 3 (2018) 1800331.
- [25] J. Xie, H. Zhang, S. Li, R. Wang, X. Sun, M. Zhou, J. Zhou, X.W. Lou, Y. Xie, Defect-rich MoS_2 ultrathin nanosheets with additional active edge sites for enhanced electrocatalytic hydrogen evolution, *Adv. Mater.* 25 (2013) 5807–5813.
- [26] Z. Zhao, F. Qin, S. Kasiraju, L. Xie, M.K. Alam, S. Chen, D. Wang, Z. Ren, Z. Wang, L.C. Grabow, J. Bao, Vertically aligned $\text{MoS}_2/\text{Mo}_2\text{C}$ hybrid nanosheets grown on carbon paper for efficient electrocatalytic hydrogen evolution, *ACS Catal.* 7 (2017) 7312–7318.
- [27] P.L. Qin, G.J. Fang, W.J. Ke, F. Cheng, Q. Zheng, J.W. Wan, H.W. Lei, X.Z. Zhao, In situ growth of double-layer $\text{MoO}_3/\text{MoS}_2$ film from MoS_2 for hole-transport layers in organic solar cell, *J. Mater. Chem. A* 2 (2014) 2742–2756.
- [28] L. Li, Z.D. Qin, L. Ries, S. Hong, T. Michel, J. Yang, C. Salameh, M. Bechelany, P. Miele, D. Kaplan, M. Chhowalla, D. Voiry, Role of sulfur vacancies and undercoordinated Mo regions in MoS_2 nanosheets toward the evolution of hydrogen, *ACS Nano* 13 (2019) 6824–6834.
- [29] C.J. Chen, V. Veeramani, Y.H. Wu, A. Jena, L.C. Yin, H. Chang, S.F. Hu, R.S. Liu, Phosphorous-doped molybdenum disulfide anchored on silicon as an efficient catalyst for photoelectrochemical hydrogen generation, *Appl. Catal. B: Environ.* 263 (2020), 118259.
- [30] J. Wang, L. Chen, W. Lu, M. Zeng, L. Tan, F. Ren, C. Jiang, L. Fu, Direct growth of molybdenum disulfide on arbitrary insulating surfaces by chemical vapor deposition, *RSC Adv.* 5 (2015) 4364–4367.
- [31] K. Ojha, M. Sharma, H. Kolev, A.K. Ganguli, Reduced graphene oxide and MoP composite as highly efficient and durable electrocatalyst for hydrogen evolution in both acidic and alkaline media, *Catal. Sci. Technol.* 7 (2017) 668–676.
- [32] C.H. Lee, S. Lee, G.S. Kang, Y.K. Lee, G.G. Park, D.C. Lee, H.I. Joh, Insight into the superior activity of bridging sulfur-rich amorphous molybdenum sulfide for electrochemical hydrogen evolution reaction, *Appl. Catal. B: Environ.* 258 (2019), 117959.
- [33] Z.X. Wu, J. Wang, K.D. Xia, W. Lei, X. Liu, D.L. Wang, $\text{MoS}_2\text{-MoP}$ heterostructured nanosheets on polymer-derived carbon as an electrocatalyst for hydrogen evolution reaction, *J. Mater. Chem. A* 6 (2018) 616–622.
- [34] D. Zhu, L. Zhang, R.E. Ruther, R.J. Hamers, Photo-illuminated diamond as a solid-state source of solvated electrons in water for nitrogen reduction, *Nat. Mater.* 12 (2013) 836–841.
- [35] X. Cheng, J.W. Wang, W. Xiong, T. Wang, T.W. Wu, S.Y. Lu, G. Chen, S.Y. Gao, X. F. Shi, Z.N. Jiang, X.B. Niu, X.P. Sun, Greatly enhanced electrocatalytic N_2 reduction over $\text{V}_2\text{O}_3/\text{C}$ by P doping, *ChemNanoMat* 6 (2020) 1315–1319.
- [36] T. Wang, S.X. Li, B.L. He, X.J. Zhu, Y.L. Luo, Q. Liu, T.S. Li, S.Y. Lu, C. Ye, A. M. Asiri, X.P. Sun, Commercial indium-tin oxide glass: a catalyst electrode for efficient N_2 reduction at ambient conditions, *Chin. J. Catal.* 42 (2021) 1024–1029.
- [37] C. Lv, C. Yan, G. Chen, Y. Ding, J. Sun, Y. Zhou, G. Yu, An amorphous noble-metal-free electrocatalyst that enables nitrogen fixation under ambient conditions, *Angew. Chem. Int. Ed.* 57 (2018) 6073–6076.
- [38] H.H. Xian, H.R. Guo, J.J. Xia, Q.R. Chen, Y.L. Luo, R. Song, T.S. Li, E. Traversa, Iron-doped MoO_3 nanosheets for boosting nitrogen fixation to ammonia at ambient conditions, *ACS Appl. Mater. Interfaces* 13 (2021) 7142–7151.

[39] S.X. Li, Y.Y. Wang, J. Liang, T. Xu, D.W. Ma, Q. Liu, T.S. Li, S.R. Xu, G. Chen, A. M. Asiri, Y.L. Luo, Q. Wu, X.P. Sun, TiB₂ thin film enabled efficient NH₃ electrosynthesis at ambient conditions, *Mater. Today Phys.* 18 (2021), 100396.

[40] J. Han, X. Ji, X. Ren, G. Cui, L. Li, F. Xie, H. Wang, B. Li, X. Sun, MoO₃ nanosheets for efficient electrocatalytic N₂ fixation to NH₃, *J. Mater. Chem. A* 6 (2018) 12974–12977.

[41] M.M. Shi, D. Bao, B.R. Wulan, Y.H. Li, Y.F. Zhang, J.M. Yan, Q. Jiang, Au sub-nanoclusters on TiO₂ toward highly efficient and selective electrocatalyst for N₂ conversion to NH₃ at ambient conditions, *Adv. Mater.* 29 (2017), 1606550.

[42] C. Lv, Y. Qian, C. Yan, Y. Ding, Y. Liu, G. Chen, G. Yu, Defect engineering metal-free polymeric carbon nitride electrocatalyst for effective nitrogen fixation under ambient conditions, *Angew. Chem. Int. Ed.* 57 (2018) 10246–10250.

[43] C. He, Z.Y. Wu, L. Zhao, M. Ming, Y. Zhang, Y. Yi, J.S. Hu, Identification of FeN₄ as an efficient active site for electrochemical N₂ reduction, *ACS Catal.* 9 (2019) 7311–7317.

[44] S.Z. Andersen, V. Čolić, S. Yang, J.A. Schwalbe, A.C. Nielander, J.M. McEnaney, K. Enemark-Rasmussen, J.G. Baker, A.R. Singh, B.A. Rohr, M.J. Statt, S.J. Blair, S. Mezzavilla, J. Kibsgaard, P.C.K. Vesborg, M. Cargnello, S.F. Bent, T.F. Jaramillo, I.E.L. Stephens, J.K. Nørskov, I. Chorkendorff, A rigorous electrochemical ammonia synthesis protocol with quantitative isotope measurements, *Nature* 570 (2019) 504–508.

[45] C.K. Choi, G.H. Gu, J. Noh, H.S. Park, Y.S. Jung, Understanding potential-dependent competition between electrocatalytic dinitrogen and proton reduction reactions, *Nat. Commun.* 12 (2021) 4353–4363.

[46] B.H.R. Suryanto, H.L. Du, D.B. Wang, J. Chen, A.N. Simonov, D.R. MacFarlane, Challenges and prospects in the catalysis of electroreduction of nitrogen to ammonia, *Nat. Catal.* 2 (2019) 290–296.

[47] X. Ren, X. Ji, Y. Wei, D. Wu, Y. Zhang, M. Ma, Z. Liu, A.M. Asiri, Q. Wei, X. Sun, In situ electrochemical development of copper oxide nanocatalysts within a TCNQ nanowire array: a highly conductive electrocatalyst for the oxygen evolution reaction, *Chem. Commun.* 54 (2018) 1425–1428.

[48] X. Ren, R. Ge, Y. Zhang, D. Liu, D. Wu, X. Sun, B. Du, Q. Wei, Cobalt-borate nanowire array as a high-performance catalyst for oxygen evolution reaction in near-neutral media, *J. Mater. Chem. A* 5 (2017) 7291–7294.

[49] J. Zhao, X. Ren, H. Ma, X. Sun, Y. Zhang, T. Yan, Q. Wei, D. Wu, Synthesis of self-supported amorphous CoMoO₄ nanowire array for highly efficient hydrogen evolution reaction, *ACS Sustain. Chem. Eng.* 5 (2017) 10093–10098.

[50] R. Zhang, X. Ren, X. Shi, F. Xie, B. Zheng, X. Guo, X. Sun, Enabling effective electrocatalytic N₂ conversion to NH₃ by the TiO₂ nanosheets array under ambient conditions, *ACS Appl. Mater. Interfaces* 10 (2018) 28251–28255.

[51] D.X. Zhang, Y.H. Liu, B.D. Mao, H.T. Li, T.Y. Jiang, D.Q. Zhang, W.X. Dong, W. D. Shi, Double-phase heterostructure within Fe-doped Cu_{2-x}S quantum dots with boosted electrocatalytic nitrogen reduction, *ACS Sustain. Chem. Eng.* 9 (2021) 2844–2853.

[52] Y. Wei, X. Ren, H. Ma, X. Sun, Y. Zhang, X. Kuang, T. Yan, H. Ju, D. Wu, Q. Wei, CoC₂O₄ center derived Co₃O₄ nanorods array: a high-efficiency 1D electrocatalyst for alkaline oxygen evolution reaction, *Chem. Commun.* 54 (2018) 1533–1536.

[53] J. Zhao, X. Ren, Q. Han, D. Fan, X. Sun, X. Kuang, Q. Wei, D. Wu, Ultra-thin wrinkled NiOOH-NiCr₂O₄ nanosheets on Ni foam: an advanced catalytic electrode for oxygen evolution reaction, *Chem. Commun.* 54 (2018) 4987–4990.

[54] D. Wu, Y. Wei, X. Ren, X. Ji, Y. Liu, X. Guo, Z. Liu, A.M. Asiri, Q. Wei, X. Sun, Co(OH)₂ nanoparticle-encapsulating conductive nanowires array: room-temperature electrochemical preparation for high-performance water oxidation electrocatalysis, *Adv. Mater.* 3 (2018) 1705366.

[55] C. Chen, K.C. Yang, M. Basu, T.H. Lu, Y.R. Lu, C.L. Dong, S.F. Hu, R.S. Liu, Wide range pH-tolerable silicon@pyrite cobalt dichalcogenide microwire array photoelectrodes for solar hydrogen evolution, *ACS Appl. Mater. Interfaces* 8 (2016) 5400–5407.

[56] Y.P. Li, L.Y. Huang, J.B. Xu, H. Xu, Y.G. Xu, J.X. Xia, H.M. Li, Visible-light-induced blue MoO₃-C₃N₄ composite with enhanced photocatalytic activity, *Mater. Res. Bull.* 70 (2015) 500–505.

[57] J. Zhang, X.Y. Tian, M.J. Liu, H. Guo, J.D. Zhou, Q.Y. Fang, Z. Liu, Q. Wu, J. Lou, Cobalt-modulated molybdenum-dinitrogen interaction in MoS₂ for catalyzing ammonia synthesis, *J. Am. Chem. Soc.* 141 (2019) 19269–19275.

[58] W.R. Liao, K. Xie, L.J. Liu, X.Y. Wang, Y. Luo, S.J. Liang, F.J. Liu, L.L. Jiang, Triggering in-plane defect cluster on MoS₂ for accelerated dinitrogen electroreduction to ammonia, *J. Energy Chem.* 62 (2021) 359–366.

[59] B.L. Zhao, J. Huang, Q. Fu, L. Yang, J.Y. Zhang, B. Xiang, MoS₂/NbSe₂ hybrid nanobelts for enhanced hydrogen evolution, *Electrochim. Soc.* 163 (2016) H384–H387.

[60] J.J. Xia, H.R. Guo, M.Z. Cheng, C.Y. Chen, M.K. Wang, Y. Xiang, T.S. Li, E. Traversa, Electrospun zirconia nanofibers for enhancing the electrochemical synthesis of ammonia by artificial nitrogen fixation, *J. Mater. Chem. A* 9 (2021) 2145–2151.